Commun. Comput. Phys.
doi: 10.4208/cicp.221209.250510a

Vol. **9**, No. 2, pp. 269-296
February 2011

Lattice Boltzmann Methods for Multiphase Flow Simulations across Scales

Giacomo Falcucci[1], Stefano Ubertini[1], Chiara Biscarini[3,5], Silvia Di Francesco[3,6], Daniele Chiappini[2], Silvia Palpacelli[7], Alessandro De Maio[7] and Sauro Succi[4,*]

[1] *Department of Technologies, University of Naples "Parthenope", Centro Direzionale-Isola C4, 80143 Naples, Italy.*
[2] *Department of Mechanical Engineering, University of Rome "Tor Vergata", Viale Politecnico, Rome, Italy.*
[3] *H2CU, Honors Center of Italian Universities-University of Rome "La Sapienza", Rome, Italy.*
[4] *Istituto Applicazioni Calcolo, CNR, Via dei Taurini 9, 00185 Rome, Italy.*
[5] *Water Resources Research and Documentation Centre, University for Foreigners, Villa La Colombella, Perugia, Italy.*
[6] *Department of Civil and Environmental Engineering, University of Perugia, Via G. Duranti 93, Perugia, Italy.*
[7] *Nu.M.I.D.I.A. srl, Via Berna 31, 00184 Roma, Italy.*

Received 22 December 2009; Accepted (in revised version) 25 May 2010

Available online 27 August 2010

Abstract. The simulation of multiphase flows is an outstanding challenge, due to the inherent complexity of the underlying physical phenomena and to the fact that multiphase flows are very diverse in nature, and so are the laws governing their dynamics. In the last two decades, a new class of mesoscopic methods, based on minimal lattice formulation of Boltzmann kinetic equation, has gained significant interest as an efficient alternative to continuum methods based on the discretisation of the NS equations for non ideal fluids. In this paper, three different multiphase models based on the lattice Boltzmann method (LBM) are discussed, in order to assess the capability of the method to deal with multiphase flows on a wide spectrum of operating conditions and multiphase phenomena. In particular, the range of application of each method is highlighted and its effectiveness is qualitatively assessed through comparison with numerical and experimental literature data.

PACS: 47.11.-j, 47.65.Cb

Key words: Lattice Boltzmann, multiphase flows.

*Corresponding author. *Email addresses:* giacomo.falcucci@uniparthenope.it (G. Falcucci), stefano.ubertini@uniparthenope.it (S. Ubertini), biscarini.chiara@unistrapg.it (C. Biscarini), silvia.difrancesco@unipg.it (S. Di Francesco), chiappini@ing.uniroma2.it (D. Chiappini), demaio@numidia.rm.it (A. De Maio), succi@iac.cnr.it (S. Succi)

1 Introduction

The understanding of multiphase flows across space-time scales has always been of great interest both from a theoretical and a practical point of view. A number of industrial and technological processes are, in fact, associated with dispersed or separated multiphase flows, over a wide spectrum of different scales. Micro and nanometric multiphase flows play a crucial role in many emerging applications in material science, chemistry, engineering and biology. Similarly, the macroscopic phenomena related to multiphase fluid dynamics are also particularly important in many engineering areas, from cavitating pumps and turbines to water waves formation and propagation. A deeper understanding of the physics of fluids and the ability of predicting the fluid flow behaviour in such engineering processes is of paramount importance to these applications. However, the simulation of the above phenomena is a great challenge due to the inherent complexity of the involved phenomena (emergence of moving interfaces with complex topology, droplet collision and break-up), and represents one of the leading edges of computational physics [1]. A general computational approach encompassing the full spectrum of complexity exposed by multiphase flows is not available, yet. This is a consequence of the variety of phase combinations and interphase interactions and processes (i.e., viscosity, surface tension, heat conduction, phase transition, fragmentation and coagulation of drops and bubbles) which affect the physics of multiphase flows. The numerical methods based on the traditional continuum approach (i.e., Navier-Stokes with closure relationships) usually rely upon rather complex correlations and often require transient solution algorithms with very small time steps. In the last two decades, a new class of mesoscopic methods, based on minimal lattice formulation of Boltzmann kinetic equation, have gained significant interest as an efficient alternative to continuum methods based on the discretisation of the NS equations for non ideal fluids [2]. Since its early days, the Lattice Boltzmann shed promises of becoming a valuable tool for the modeling of multiphase flows. The continuum approach, in fact, may become inadequate to describe complex flow phenomena (i.e., droplet formation, break-up, cavitation and coalescence, water waves and free-surface flows) associated to the contemporary presence of different phases. Such difficulties are often signalled by a singular behaviour of the continuum equations (i.e., tip rupture) [3]. The kinetic approach is in principle better suited to handle the complex phenomena related to multiphase flows, since it can incorporate (minimal) aspects of microscopic physics (i.e., interphase interactions) without surrendering the computational efficiency of continuum methods.

With concern to the latter point, it is worth noting that a still widespread misbelief is that LBE should apply only to dilute gases, the reason being that it derives from an approximation of the continuum Boltzmann equation, which was originally derived under the assumption of dilutedness. This line of thinking fails to recognize that, although kinetic theory was originally meant to describe weakly-interacting (dilute) systems, it can also be applied whenever strong interactions between elementary degrees of freedom can be cast in the form of weak interactions between appropriate collective degrees of

freedom (quasi-particles). LB falls within this category, since each LB population is hydrodynamically representative of a large collection of real molecules. Another source of confusion is to assume that, since BGK is a model approximation to the true Boltzmann equation, it should inherit all of its limitations. This is not necessarily the case, because BGK is based on two fairly universal assumptions, namely

1. there exist a local attractor to the collisional dynamics (local equilibrium),

2. in the vicinity of this local equilibrium, the collisional dynamics can be described in terms of a simple relaxation process, the relaxation time-scale fixing the viscosity of the fluid.

Assumption 1 is certainly true for any statistical-dynamics system supporting microscopic invariants, while Assumption 2 is also fairly plausible for generic systems with short-range interactions. For sure, neither of the two is restricted to dilute gases.

The earliest Lattice Boltzmann simulations of multi-component flows have been performed by Gunstensen et al. [4,5] and Grunau et al. [2], based on the pioneering Rothman-Keller lattice gas multi-phase model [6]. Ever since, many models have been proposed in the past in order to simulate multiphase flows with the LBM, most of them aiming at incorporating the physics of phase-segregation and interface dynamics, typically hard to model with traditional methods, through simple mesoscopic interaction laws. To date, there are several methods to incorporate the physics of complex non-ideal fluids at the kinetic (Lattice Boltzmann) levels. In this paper, we shall focus on the following three classes, restricting our attention to *single-component multi-phase* flows only:

- Pseudo-Potential (PP);
- Free-Energy (FE);
- Front-Tracking (FT).

Pseudo-potential methods are based on the explicit representation of non-ideal forces acting in the fluid based on very general symmetry requirements. Free-energy methods, on the other hand, owe their name to the fact that non-ideal forces are derived from a first-principle free-energy functional of the fluid density.

Both PP and FE methods belong to the general class of *diffuse-interface* (DI) methods, whereby the interface between the two phases is not tracked explicitly, but rather defined by the transition region of a given scalar function, typically the fluid density or an equivalent scalar. By definition, this implies that the interface extends over a number of grid sites, whence the denomination "diffuse-interface". The FT method belongs instead to the so-called class of front-tracking (FT) methods, whereby the interface is explicitly tracked within the grid. In these methods, the interface is basically a zero-thickness mathematical surface, hosting a discontinuous jump of the fluid density across the light and dense phases, say vapor and liquid. Since no effort is spent in describing the internal structure of the front, it is clear that front-tracking methods are most naturally addressed to large-scale flows, whereas diffuse-interface methods can, in principle, account for the physics of the phase-transition across the interface, so that they are most naturally targeted to smaller scales. Conceptually, DI and FT methods fall within the general rubric of

Eulerian versus Lagrangian methods, respectively. From the computational standpoint, diffuse-interface methods are simpler, because they do not require any front tracking and reconstruction within the grid, but are exposed to the usual weaknesses of Eulerian methods, high-resolution to tame excessive numerical diffusivity. Lagrangian methods on the other hand, are more exposed to numerical instabilities generated by geometrical complexities of the moving interface. Consistently with the mesoscopic nature of kinetic theory, to date LB methods have been used almost exclusively in their DI versions. However, recent work, including the one presented here, is starting to appear also in the FT camp. That is basically the motivation for the "across" in the title of the present paper.

This paper presents selected applications, directly drawn from the authors first-hand experience, of the three aforementioned LBM approaches to multiphase flows, covering a broad range of spatial scales. No attempt is made to couple these methods across scales [7], but special attention is paid instead to a qualitative identification of the parametric regimes in which each of these models is possibly best applied.

The paper is organized as follows. After a brief introduction to the Lattice Boltzmann method, the description of the three different multi-phase approaches is presented. For each method, the field of application and related numerical results are reported. Finally, some qualitative conclusions on their range of practical applicability are drawn. Needless to say, these conclusions reflect the author's own specific experience and not meant to bear more generality than this.

2 The lattice Boltzmann method

The Lattice Boltzmann method is based on the following evolution equation for the discrete one-particle Boltzmann distribution

$$\frac{\partial f_\alpha}{\partial t} + \boldsymbol{c}_\alpha \cdot \nabla f_\alpha = -\frac{1}{\tau_0}(f_\alpha - f_\alpha^{eq}), \tag{2.1}$$

where $f_\alpha(\boldsymbol{x},t)$ is the probability of finding a particle at the site $\boldsymbol{x}$ and time t moving with velocity $\boldsymbol{c}_\alpha$ (9 for 2D simulation and 15 or 19 for 3D [8]) associated with a uniform Cartesian lattice. In Eq. (2.1), τ_0 is the (single) relaxation time and $f_\alpha^{eq}(\mathbf{x},t)$ is the equilibrium distribution function depending of the macroscopic variables of the flow. This is given by

$$f_\alpha^{eq} = \rho w_\alpha \left(1 + \frac{\boldsymbol{c}_\alpha \cdot \boldsymbol{u}}{c_s^2} + \frac{(\boldsymbol{c}_\alpha \cdot \boldsymbol{u})^2}{2c_s^4} - \frac{(\boldsymbol{u}\cdot\boldsymbol{u})}{2c_s^2}\right), \tag{2.2}$$

Eq. (2.1) upon explicit time integration, delivers

$$f_\alpha(\boldsymbol{x}+\boldsymbol{c}_\alpha\Delta t, t+\Delta t) - f_\alpha(\boldsymbol{x},t) = -\frac{\Delta t}{\tau}(f_\alpha - f_\alpha^{eq}). \tag{2.3}$$

Physical quantities such as density ρ and fluid velocity $\boldsymbol{u}$ are defined as moments of f_α [9], as follows:

$$\rho(\boldsymbol{x},t)=\sum_{\alpha=0}^{N-1} f_\alpha(\boldsymbol{x},t), \tag{2.4a}$$

$$\rho\boldsymbol{u}(\boldsymbol{x},t)=\sum_{\alpha=0}^{N-1} \boldsymbol{c}_\alpha f_\alpha(\boldsymbol{x},t), \tag{2.4b}$$

where N is the number of discrete speeds, including a zero-speed rest particle.

In the limit of weak departures from local equilibrium (i.e., small *Knudsen* numbers) and near the incompressible limit (small *Mach* numbers), it can be shown [9] through the Chapman-Enskog expansion that the above formulation recovers the dynamic behaviour of a fluid with pressure $P=c_s^2\,\rho$ and kinematic viscosity given by $\nu=c_s^2(\tau-\Delta t/2)$, where c_s^2 is the lattice sound speed, $c_s^2=\sum_\alpha |c_\alpha|^2/D$, in D spatial dimensions.

2.1 Interphase interactions

The LB method allows to account for the interactions between different phases in non-ideal fluids, by means of a generalized streaming term in velocity space, associated with the presence of a generic force $\boldsymbol{F}$ at the left-hand side of the Eq. (2.1)

$$\frac{\boldsymbol{F}}{m}\cdot\frac{\partial f}{\partial \vec{v}}. \tag{2.5}$$

The force $\boldsymbol{F}$ accounts for *both* external fields (such as gravity or electro-magnetic fields) and *self-consistent* forces associated with intermolecular interactions. The corresponding generalized Lattice Bathnagar-Gross-Krook (LBGK) equation reads as follows:

$$f_\alpha(\boldsymbol{x}+\boldsymbol{c}_\alpha\Delta t,t+\Delta t)-f_\alpha(\boldsymbol{x},t)=-\frac{\Delta t}{\tau}(f_\alpha-f_\alpha^{eq})+F_\alpha\Delta t, \tag{2.6}$$

where the source term F_α can be formally interpreted as the discrete velocity representation of (2.5). Different formulations of the term F_α give rise to a variety of different multiphase approaches within the Lattice Boltzmann scenario.

3 The pseudo-potential approach

The pseudopotential method put forward a decade ago by Shan and Chen to endow Lattice Boltzmann (LB) models with potential energy interactions, is one of the most successful outgrowths of basic LB theory [10, 11]. The Shan-Chen (SC) model is based on the idea of representing intermolecular interactions at the mesoscopic scale via a density-dependent nearest-neighbor pseudo-potential $\psi(\rho)$. Despite its highly simplified character, the SC model provides the essential ingredients of non-ideal (dense) fluid behaviour, that is, a non-ideal equation of state; surface tension effects at phase interfaces.

The lattice Boltzmann (LB) equation with pseudo-potentials takes the following form ($\Delta t=1$ for simplicity):

$$f_\alpha(\boldsymbol{x}+\boldsymbol{c}_\alpha,t+1)-f_\alpha(\boldsymbol{x},t)=-\omega(f_\alpha-f_\alpha^{eq})+F_\alpha. \tag{3.1}$$

The term F_α derives form the following force:

$$\boldsymbol{F}(\boldsymbol{x},t)=-G_0\psi(\boldsymbol{x},t)\sum_{\alpha=1}^{N_f}w_\alpha\psi(\boldsymbol{x}+\boldsymbol{c}_\alpha,t)\boldsymbol{c}_\alpha, \tag{3.2}$$

where N_f is the number of lattice links associated with the spatial range of the pseudo-potential $\psi(\boldsymbol{x},t)$ (9 in the standard SC approach) and G_0 is the strength of the interparticle interactions. The pseudo-potential $\psi(\boldsymbol{x},t)$ is typically chosen as a local functional of fluid density, as follows:

$$\psi(\boldsymbol{x},t)=\rho_0\Big[1-\exp\Big(-\frac{\rho(\boldsymbol{x},t)}{\rho_0}\Big)\Big]. \tag{3.3}$$

Note that positive (negative) G_0 codes for repulsion/attraction, respectively. The latter case is the one relevant to phase-separating scenarios. In the following, the reference density ρ_0 is set to $\rho_0=1$ for the sake of simplicity. Also to be noted that G_0 is the only free parameter, fixing both the density ratio between the two phases (equation of state) and the surface tension of the model.

The effects of the force (3.2) are best incorporated through a shift in the fluid velocities entering the equilibrium distribution functions, according to

$$\boldsymbol{u}'(\boldsymbol{x},t)=\boldsymbol{u}(\boldsymbol{x},t)+\frac{\boldsymbol{F}(\boldsymbol{x},t)\tau}{\rho(\boldsymbol{x},t)}. \tag{3.4}$$

This shift preserves the (truncated) Maxwellian nature of the local equilibrium, which proves beneficial from both conceptual and computational points of view.

Owing to the non-ideal force, the Equation of State (EOS) takes the following form:

$$P=\rho c_s^2+\frac{c_s^2G_0}{2}\psi^2, \tag{3.5}$$

where the first term at the right-hand-side is the ideal contribution, whereas the second one accounts for non-ideal effects ("excess pressure"). Phase transitions are triggered by letting the coupling parameter exceed a given critical threshold. At a critical density $\rho_{crit}=\rho_0 log2$, phase transitions occur for $G_0<G_{crit}=-4$. The surface tension is given by

$$\sigma\sim-G_0c_s^4\int(\nabla_y\Psi)^2dy, \tag{3.6}$$

where y runs across the (plane) interface between the two phases.

The SC method shines for its elegance and simplicity, but it also comes with a number of practical restrictions.

First, being a diffuse-interface method, the interphase boundary extends over a few mesh spacings, typically

$$\frac{\delta}{\Delta x}\sim 5, \tag{3.7}$$

δ being the interface width. This implies an obvious constraint in terms of mesh resolution. In fact, most physical interfaces extend over nanometric distances, the typical range of molecular interactions, which means that a quantitative description of the interface physics would require nanometric mesh-spacings. Generally, LB is not meant to describe such nanoscopic scales, and consequently the mesh interface in LB calculations is typically 2-3 orders of magnitude thicker than real ones. Fortunately, the large scale features of the flow are often largely insensitive to this artificial upscaling. For instance, numerical experiments on capillary flows show that the penetration of the capillary front sets to its thin-interface ($\delta\to 0$) value at $\delta/H<0.1$, H being a macroscopic scale of the problem [12]. With

$$\frac{\delta}{\Delta x}\sim 5, \qquad N=\frac{H}{\Delta x}\sim\mathcal{O}(100),$$

grid points are typically sufficient to tame finite-thickness interface effects. Of course, this cannot be taken as a general rule, and caution must be taken to assess this sensitivity case-by-case.

A second limitation concerns the density jump across the interface. The standard version is limited to moderate density ratios, usually around $\rho_L/\rho_V\leq 50-100$. Beyond such values, spurious currents, due to the lack of high-order isotropy of the forcing term, usually lead to destructive instabilities. Fortunately, many applications are rather insensitive to the specific value of the density ratio, so long this is well above 10. Again, this statement must be checked case-by-case, depending on the physics under inspection.

There is another concern of thermodynamic nature. The only choice for which mechanical stability of the interface is compatible with the thermodynamic Maxwell's area-rule, is

$$\psi(\rho)=\rho.$$

However, in the absence of a repulsive core, this choice inevitably leads to "mass collapse", with a boundless build-up of the particle density. In the SC formulation, Eq. (3.3), such density collapse is prevented by the saturation of ψ at $\rho\gg\rho_0$, leading to a vanishing force whenever the fluid density significantly exceeds the reference one. Numerical practice shows that the effects of this artificial saturation on the Maxwell-rule is numerically negligible under most conditions of practical interest. This largely voids the keen criticism raised against the PP method, as being incompatible with thermodynamic fundamentals.

Notwithstanding the above limitations, in view of its remarkable computational simplicity, the SC method is being used for a growing body of complex flows applications, such as multiphase flows in chemical, manufacturing and also geophysical problems [13, 14].

3.1 The multi-range pseudo-potential approach

Modern variants [15–17] considerably extend the scope of the original SC model. As described in [15], it is possible to consider *multi-range* expressions of the form

$$\boldsymbol{F}(\boldsymbol{x},t)=c_s^2\sum_{j=1}^{2}G_j\psi_j\left[\rho(\boldsymbol{x},t)\right]\sum_{\alpha=1}^{b_j}p_{\alpha j}\boldsymbol{c}_{\alpha j}\psi_j\left[\rho(\boldsymbol{x}+\boldsymbol{c}_{\alpha j},t)\right]. \tag{3.8}$$

In the above, the index j labels the Seitz-Wigner cell (*belt* for simplicity) defined by the condition $|\boldsymbol{x}'-\boldsymbol{x}|^2\leq 2j^2$, whereas $\boldsymbol{c}_{\alpha j}$ denotes the set of discrete speeds belonging to the j-th belt. Note that lattice units $\Delta x=\Delta t=1$ have been assumed here. In this work, we shall confine our attention to the 24-neighbors, 2-belt lattice depicted in Fig. 1.

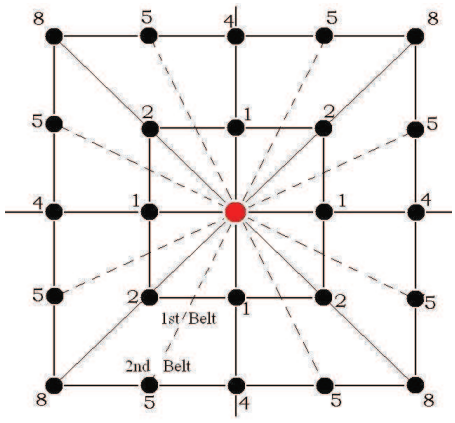

Figure 1: Two-belt lattice for force evaluation. Each node is labelled by the corresponding energy $|c_{\alpha j}|^2$. Belt 1 contains eight speeds and two energy levels $(1,2)$. Belt 2 contains sixteen speeds, distributed over three energy levels $(4,5,8)$.

As is well-known, the standard 1-belt, 8-speed lattice provides isotropy of the 4th-order kinetic tensor $\sum_i \boldsymbol{c}_i\boldsymbol{c}_i\boldsymbol{c}_i\boldsymbol{c}_i$, corresponding to 2nd-order isotropic hydrodynamics, whereas the 2-belts, 24-speed lattice upgrades isotropy to 8th order, provided the weights are properly chosen. A suitable choice is reported in [15]. We wish emphasize that the 2-belt lattice is used *only* for the (pseudo)-force evaluation, whereas the standard lattice Boltzmann dynamics still takes place in the original nine speed, two-dimensional lattice (D2Q9). This is also the reason why we keep a separate notation for the weights w_α used for the lattice Boltzmann populations and the weights $p_{\alpha j}$ used for the force evaluation. The equation of state of our system, reads as follows:

$$p(\rho)=\rho c_s^2+\frac{1}{2}G^{(2)}\psi^2, \tag{3.9}$$

where

$$G^{(2)}=G_1C_1+G_2C_2, \tag{3.10}$$

is an effective coupling and

$$c_s^2=\sum_{\alpha=0}^{8} w_\alpha c_{\alpha 1,x}^2=\frac{1}{3},\quad C_1=\sum_{\alpha=1}^{8} p_{\alpha 1} c_{\alpha 1,x}^2=\frac{737}{3000},\quad C_2=\sum_{\alpha=1}^{16} p_{\alpha 2} c_{\alpha 2,x}^2=\frac{33}{375}.$$

At the level of the EOS, this is the same as the Shan-Chen model, just with a rescaled coupling. However, since repulsive forces act also on the second belt of neighbors, they are distributed differently in space, and consequently their effect cannot be captured by a mere rescaling of the attractive interactions, possibly allowing density ratios to depend on G_1 and G_2 separately. Taylor-expansion of Eq. (3.8) to 4-th order in Δt delivers the following continuum force:

$$\boldsymbol{F}(\boldsymbol{x},t)=G^{(2)}\Psi\boldsymbol{\nabla}\psi+G^{(4)}\Psi\boldsymbol{\nabla}\nabla^2\psi+\mathcal{O}(\nabla^4), \tag{3.11}$$

where

$$G^{(4)}=G_1\sum_{\alpha=1}^{8} p_{\alpha 1} c_{\alpha x}^4+G_2\sum_{\alpha=1}^{16} p_{\alpha 2} c_{\alpha x}^4.$$

This expression differs from standard Shan-Chen, for which $G^{(2)}=G_1$ and $G_2=0$. The two-parameter equation of state (3.9) offers an additional degree of freedom, G_2, as compared with the standard Shan-Chen. As recently shown [16], this degree of freedom can be used to tune the surface tension independently of the equation of state. The extension to the second belt of the interphase interaction allows several enhancements, as compared to the standard Shan-Chen approach. The density ratio can raise up to 1:250, only limited by the magnitude of parasitic currents which, at high density ratios, can grow up to $u_{spurious}\sim 0.3$. The presence of two free parameters, namely G_1 and G_2 permits to control the surface tension magnitude for a given density ratio, which is not possible in the standard Shan-Chen approach. In particular, by choosing repulsive interactions in the second belt ($G_2>0$), it is possible to achieve substantial reduction of the surface tension, thereby allowing the onset of long-lived metastable droplets. Moreover, the $2-belt$ approach offers the possibility to reduce the magnitude of spurious currents nearly an order of magnitude [18].

3.2 Pseudo-potential method: simulations and results

The Pseudo-Potential approach can be conveniently used to study the wettability of solid surfaces and the behaviour of droplets impinging on wet or dry (hydrophobic or hydrophilic) surfaces. Fig. 2 reports the comparison of the deformation of a droplet impinging on a dry hydrophobic surface (Fig. 2(b)) with the experimental measures performed by Clanet et al. [19]. The case reported in the left panel in Fig. 2 is characterized by $Re_L\sim 20$ and $We_L\sim 12$, where the subscript L indicates that the non-dimensional parameters are calculated on the heavy (i.e., liquid) fluid properties; the density ratio between the two phases is $\rho_L/\rho_V\sim 15$. The definition of Re and We numbers are standard, see

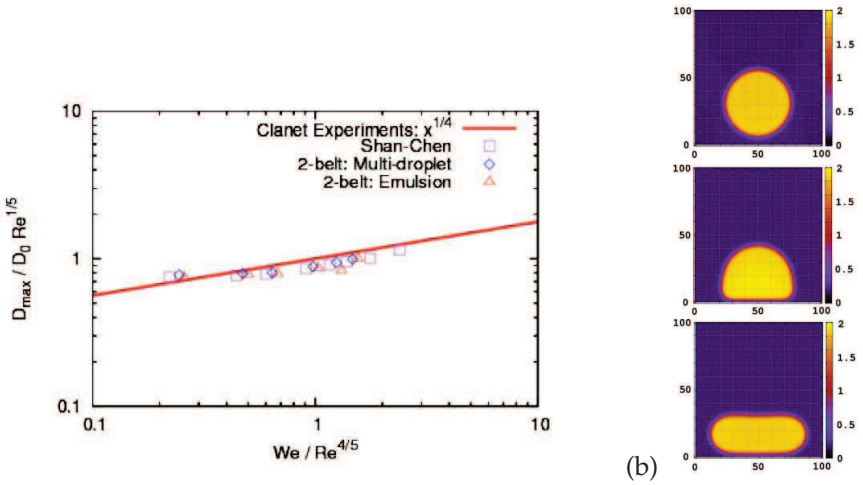

Figure 2: (a) Comparison between the droplet deformations computed with the LB method and the experimental results obtained by Clanet et al. [19]; (b) Sketch of drop impact on a hydrophobic wall.

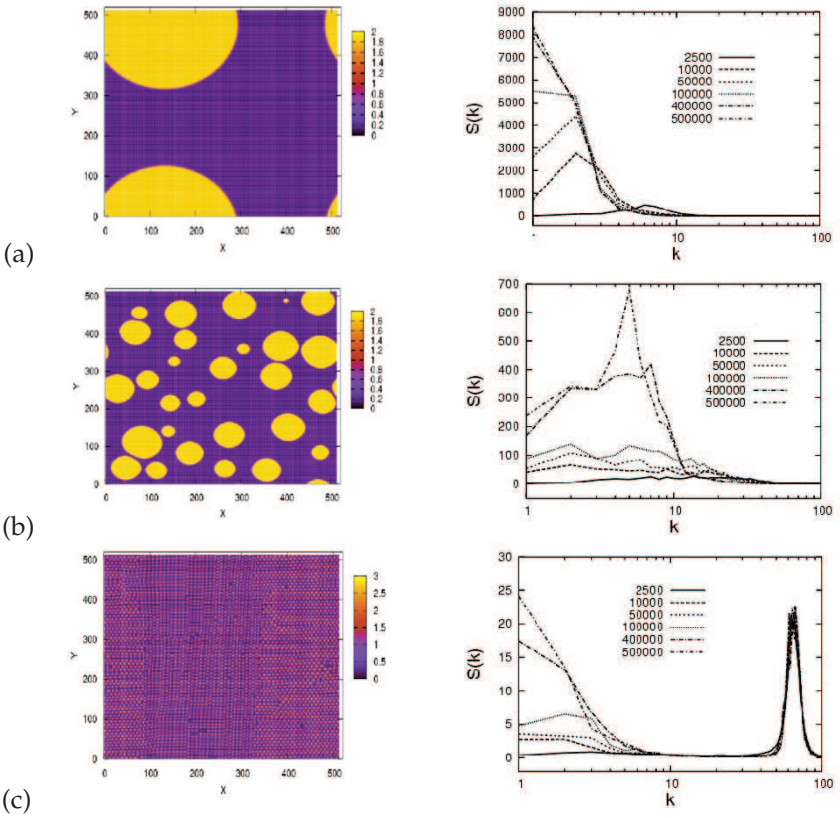

Figure 3: Spatial distribution of the fluid density. The formation of a large number of droplets with increasing G_2 is well visible. (a): Standard Shan-Chen, $G_1=4.90$, $G_2=0.0$, grid size 512×512, t=500 000; (b): Multidroplet, $G_1=-15.00$, $G_2=10.1$, grid size 512×512, t=500 000; (c): Emulsion, $G_1=-18.00$, $G_2=14.1$, grid size 512×512, t=500 000.

in sequel. The matching between the LB simulations and the experimental data is pretty satisfactory.

Besides the dynamic case in Fig. 2, we present the results obtained with the Shan-Chen and the $2-belt$ methods for a static case, characterized by a density ratio between the two phases $\rho_L/\rho_V \sim 15$ and by the dimensionless parameters $Re_L = 0$ and $We_L = 0$. Fig. 3 shows the results obtained with the *Pseudo-Potential* approach in the two versions, the standard Shan-Chen and the *2-belts*. The right-hand panel in Fig. 3 shows the Fourier spectrum of density fluctuations. Such spectrum, initially a *white noise*, evolves towards a shape peaked at the (inverse) size of the droplets. These Fourier spectra show that small-scale contribution is significantly higher when increasing the midrange repulsion, that is G_2, indicating the formation of long-lived metastable states in the form of small droplets. In particular in the last picture (d), at the end of the simulation there is a clear peak at $R \sim L/2k \approx 30$ [20]. It is possible to see the difference in the coalescence behaviour, which can be inhibited almost *ad libitum*, leading to spray-like configurations, see Fig. 3(c). Besides the sharp peak centered around the mean size of the droplets, the buildup of a low-k component with increasing G_2 is well visible, corresponding to the formation of large-scale domains indicating a higher degree of order in the global structure. The configuration presented in (c) is strongly reminiscent of a crystal, with very few defects. For these cases, the typical radius is estimated as follows: (a) $R \approx 5.1$; (b) $R \approx 4.4$; (c) $R \approx 3.9$.

The SC method has proven to be reliable and efficient in simulating multiphase phenomena at intermediate and small spatial scales, related to pressurized environments (mild density ratios between gas and liquid phase) and to study the effects of wettability of solid surfaces, such as capillary flows and wall-impingement of dense sprays. Its most recent enhancements, have also allowed the simulation of complex, spray-like fluids [15, 17, 21].

In spite of its undeniable success, the SC method has made the object of intense criticism. In particular, as mentioned previously, i) reduced density ratios, ii) spurious currents at interfaces and iii) surface tension tied-down to the equation of state, have been pointed as main limitations of the method. As discussed previously, we feel like most of this criticism can be side-stepped in actual practice. However, these limitations surely need to be constantly monitored. The spurious currents are probably the most disturbing effect for practical applications, since they can either ruin the simulation or simply cast doubts on the quantitative accuracy [22]. This explains the numerous developments aimed at coping with this problem.

4 The free energy approach

Another major route for the simulation of complex flows within a LB framework is provided by the so-called free-energy approach. As suggested by its very name, the *Free Energy* approach stems from a lattice transcription of density functional theory (Cahn-Hilliard) of non-ideal interactions [23, 24]). In its original formulation by Swift et al. [23],

the free-energy functional reads as follows:

$$\Phi(\vec{x}) = \int \left[\phi(\rho(\vec{x})) + \frac{\kappa}{2} (\nabla \rho(\vec{x}))^2 \right] d\vec{x}, \tag{4.1}$$

where the first term at the right-hand side governs the non-ideal bulk pressure, while the gradient term controls the surface tension, i.e., the cost of building an interface across the fluid. Notwithstanding their common diffuse-interface nature, the PP and FE approaches differ considerably, both in terms of their conceptual foundations and in the details of their lattice implementation.

In particular, the FE formulation can formally boast the correct thermodynamic "pedigree", for it stems directly from a free-energy functional. Nevertheless, since the PP method has been recently shown to possess an effective pseudo-free energy [25], as of today, such a distinction appears to be more academic than factual.

Unlike the standard version of PP, in the FE formulation the equation of state and the surface tension can be tuned independently. According to standard thermodynamics, the fluid pressure is given by the Legendre transform of the bulk free-energy

$$p = \rho \frac{d\Phi}{d\rho} - \rho, \tag{4.2}$$

while surface tension is controlled by the gradient parameter κ,

$$\sigma \sim \kappa \int (\nabla_y \rho)^2 dy. \tag{4.3}$$

Another technical, yet important difference between the two formulations is that in FE non-ideal interactions are not expressed through an explicit non-ideal force, but rather incorporated within a generalized equilibrium, consistent with the non-homogeneous expression of the non-ideal pressure tensor. In actual terms, this means that the local equilibrium acquires a parametric dependence on the local density gradients. However, at variance with the PP formulation, which is based on locally shifted equilibria, the FE formulation does not cast the heterogeneous equilibria in the form of a shifted-truncated Maxwellian. This might well have implications on the numerical stability of the method, although we are not aware of any quantitative comparison between the two.

As per interface thickness effects, the two formulations appear to be basically equivalent.

The free-energy approach can also boast a broad array of applications for the last fifteen years [26–32]. Since our own experience with the original FE method is pretty limited, we next move on to a recent variant of the original FE method, the so-called Finite-Difference Free-Energy method (FDFE), which appears to be particularly effective at taming the effects of spurious currents.

4.1 Finite-difference free-energy method

The FDFE method shares the conceptual foundations of the original FE ancestor, yet with a number of major technical twists, specifically aimed at taming the detrimental effects of spurious currents. Essentially, as we shall see, the idea is to devise a high-order finite difference treatment of capillary forces.

The relevant free-energy functional is formulated in terms of the of the liquid-phase concentration

$$C(\vec{x}) = \frac{\rho_L}{\rho_L + \rho_V},$$

and reads as follows:

$$E[C, \nabla C] = E_0[C] + \frac{\kappa}{2}|\nabla C|^2,$$

where κ is again the gradient parameter controlling surface tension. The bulk energy takes the form

$$E_0(C) \approx A - BC^2(C-1)^2,$$

where A is a reference energy and B is a constant fixing the free-energy barrier between the equilibrium states ($C=0$ and $C=1$). The same parameter accounts for the non-ideal bulk pressure through the Legendre's relation

$$p_0 = C\frac{\partial E_0}{\partial C} - E_0. \tag{4.4}$$

The two free parameters B and κ provide separate control of the surface tension and interface thickness, respectively,

$$\sigma = \frac{\sqrt{2\kappa B}}{6}, \qquad \delta = \sqrt{\frac{8\kappa}{B}}. \tag{4.5}$$

The external force representing the non-ideal gas effects reads as follows:

$$\mathbf{F} = \nabla \rho c_s^2 - \nabla p_0 + \rho\kappa\nabla\nabla^2\rho, \tag{4.6}$$

where the last term at the right-hand-side is directly responsible for surface tension effects.

In this respect, FDFE could be viewed as an intermediate between the original PP and FE methods: like FE, it is based on a two-parameter free-energy functional, and like PP, non-ideal interactions are represented through an explicit force. The main technical hallmark of the FDFE formulation rests with the high-order finite-difference treatment of this force, which lies at the heart of its enhanced stability versus spurious currents.

Indeed, it is well known that the numerical details of the force representation play a major role on the stability and numerical accuracy of LB formulations of non-ideal fluids [33–35].

The specific implementation due to Lee [36–39], evolves *pressure* instead of the density, and consequently, the discrete distribution function is defined as follows:

$$g_\alpha = f_\alpha c_s^2 + (p_1 - \rho c_s^2)\Gamma_\alpha(0), \tag{4.7}$$

where f_α is the usual discrete particle distribution, as defined in the classical LBE theory, and $\Gamma_\alpha(\mathbf{u}) = f_\alpha^{eq}/\rho$.

The above distribution is characterized by the following equilibrium function:

$$g_\alpha^{eq} = w_\alpha \Big[p_1 + \frac{\mathbf{c}_\alpha \cdot \mathbf{u}}{c_s^2} + \frac{(\mathbf{c}_\alpha \cdot \mathbf{u})^2}{2c_s^4} - \frac{(\mathbf{u}\cdot\mathbf{u})}{2c_s^2} \Big], \tag{4.8}$$

where p_1 is defined below, see (4.14c).

With a change of variables, useful to solve the equation within a two-step approach, the complete set of equations to be solved is

$$\bar{g}_\alpha = g_\alpha + \frac{\Delta t}{2\tau}(g_\alpha - g_\alpha^{eq}) - \frac{\Delta t}{2}(\mathbf{c}_\alpha - \mathbf{u}) \cdot \big[\nabla \rho c_s^2 (\Gamma_\alpha - \Gamma_\alpha(0)) - C\nabla\mu\Gamma_\alpha \big], \tag{4.9}$$

where the modified particle distribution reads

$$\bar{g}_\alpha^{eq} = g_\alpha^{eq} - \frac{\Delta t}{2}(\mathbf{c}_\alpha - \mathbf{u}) \cdot \big[\nabla \rho c_s^2 (\Gamma_\alpha - \Gamma_\alpha(0)) - C\nabla\mu\Gamma_\alpha \big]. \tag{4.10}$$

Second-order integration in time (Crank-Nicolson), finally leads to the following LBE for pressure field:

$$\begin{aligned} &\bar{g}_\alpha(\mathbf{x} + \mathbf{c}_\alpha \Delta t, t + \Delta t) - \bar{g}_\alpha(\mathbf{x}, t) \\ &= -\frac{1}{\tau + 0.5}(\bar{g}_\alpha - \bar{g}_\alpha^{eq})(\mathbf{x}, t) + \Delta t(\mathbf{c}_\alpha - \mathbf{u}) \cdot \big[\nabla \rho c_s^2 (\Gamma_\alpha - \Gamma_\alpha(0)) - C\nabla\mu\Gamma_\alpha \big]_{(\mathbf{x},t)}. \end{aligned} \tag{4.11}$$

The same procedure can be applied to the concentration C, by introducing a second distribution

$$h_\alpha = \frac{C}{\rho} f_\alpha, \qquad h_\alpha^{eq} = \frac{C}{\rho}\, f_\alpha^{eq},$$

which can be shown to obey the following LBE:

$$\begin{aligned} &\bar{h}_\alpha(\mathbf{x} + \mathbf{c}_\alpha \delta t, t + \delta t) - \bar{h}_\alpha(\mathbf{x}, t) \\ &= -\frac{\Delta t}{\tau + 0.5\Delta t}(\bar{h}_\alpha - \bar{h}_\alpha^{eq})(\mathbf{x}, t) + \Delta t(\mathbf{c}_\alpha - \mathbf{u}) \cdot \Big[\nabla C - \frac{C}{\rho c_s^2}(\nabla p_1 + C\nabla\mu) \Big] \Gamma_\alpha|_{(\mathbf{x},t)} \\ &\quad + \delta t \nabla \cdot (M\nabla\mu)\Gamma_\alpha|_{(\mathbf{x},t)}, \end{aligned} \tag{4.12}$$

where the modified equilibrium distribution $\bar{h}_\alpha$ and its equilibrium are calculated as in (4.9) and (4.10), namely

$$\bar{h}_\alpha^{eq} = h_\alpha^{eq} - \frac{\delta t}{2}(\mathbf{c}_\alpha - \mathbf{u}) \cdot \Big[\nabla C - \frac{C}{\rho c_s^2}(\nabla p_1 + C\nabla\mu) \Big] \Gamma_\alpha|_{(\mathbf{x},t)} - \frac{\delta t}{2} \nabla \cdot (M\nabla\mu)\Gamma_\alpha|_{(\mathbf{x},t)}. \tag{4.13}$$

In the above M is the mobility, a chemical factor which rules the rate of convergence to the equilibrium [38]. The composition, the hydrodynamic pressure and the fluid momentum are calculated by taking the zero-th and the first moments of the modified particle distribution function

$$C=\sum_{\alpha}\bar{h}_{\alpha}+\frac{\delta t}{2}\nabla\cdot(M\nabla\mu), \tag{4.14a}$$

$$\rho c_s^2\mathbf{u}=\sum_{\alpha}\mathbf{c}_{\alpha}\bar{g}_{\alpha}-\frac{\delta t}{2}C\nabla\mu, \tag{4.14b}$$

$$p_1=\sum_{\alpha}\bar{g}_{\alpha}+\frac{\delta t}{2}\mathbf{u}\cdot\nabla\rho c_s^2. \tag{4.14c}$$

The Eq. (4.14a) is non linear, however, due to the slow variation of the chemical potential on the time-scale of a single time-step, in our implementation, C at time t is updated with the value of μ at the previous time-step $t-\Delta t$, as suggested in [38]. The density and the relaxation time are calculated as local functions of the composition

$$\rho(C)=C\rho_1+(1-C)\rho_2, \tag{4.15a}$$

$$\tau(C)=C\tau_1+(1-C)\tau_2. \tag{4.15b}$$

As it is apparent from the previous equations, Lee's FDFE model is considerably more complicated and computationally demanding, than the original PP and FE methods. The reward is strong reduction of parasitic currents, hence the access to a wider range of macroscopic parameters, at least in free-flow applications, as we shall see shortly.

4.2 Finite-difference free-energy: simulations and results

The FDFE approach achieves a significant reduction of spurious currents, even in the presence of high density ratios (up to $\sim 1:1000$, but only for specific applications, involving small deformations) [40, 41].

Fig. 4(a) shows the comparison between the spike and bubble penetrations given by He et al. [42] and for the Lee model at a $Re=2048$ and Fig. 4(b) shows the evolution of the fluid interface with the Lee model. An excellent agreement with literature data is observed. The flow field is qualitatively consistent with the typical Rayleigh-Taylor instability dynamics, experimentally and numerically observed by various authors [43, 44, 47]; the initial exponential growth, the rise of the bubble of the light fluid and the spikes of denser fluid moving in the opposite direction, as well as the superficial wave breaking at a later stage of the simulation, are well visible.

5 Pseudo-potential and free-energy limitations

The LB multiphase models based on interparticle interactions (i.e., phase transitions) are subject to a number of parametric restrictions. These are best expressed in terms of di-

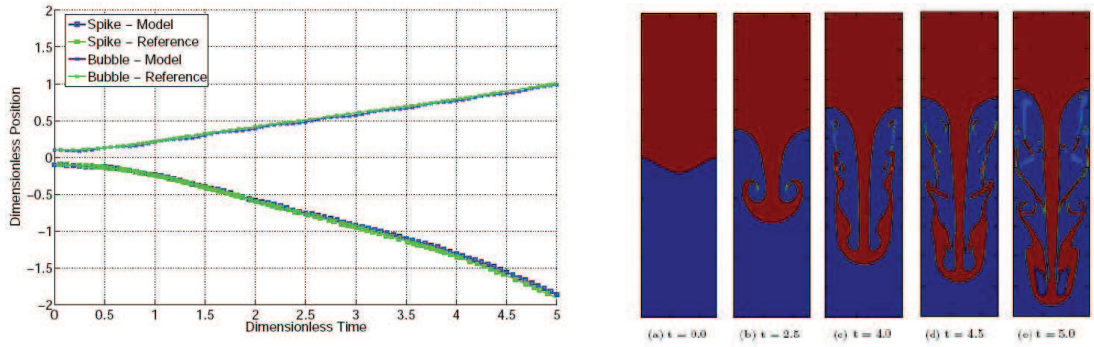

(a) (b)

Figure 4: (a): Comparison between $FDFE$ model and literature results for the liquid jet penetration. The Figure reports the dimensionless position of the spike and bubbles as a function of dimensionless time. (b): Sequence of density contours for the RT instability at different times, as computed with the Lee's model. The main parameters are: grid-size 256×1024, $Re=2048$, $At=(\rho_l-\rho_v)/(\rho_l+\rho_v)=0.5$ $(\rho_l/\rho_v\sim3)$ and $\sqrt{W\cdot g}=0.04$, with W the jet width.

mensionless parameters, measuring the relative strength of the various competing mechanisms. Among others, the most important ones are the Weber number, $We=\rho U^2D/\sigma$, measuring the competition between inertia and surface tension, the Reynolds number, $Re=UD/\nu$, measuring the ratio of inertia and dissipation, the Eotvos number $Eo=a\delta\rho D^2/\sigma$ and the Froude number $Fr=U/\sqrt{a\,D}$, expressing the relative strength of external drive (e.g., gravity) versus surface tension and inertia effects, respectively.

In the above ρ is the liquid density, U the typical speed, D the typical droplet diameter, σ the surface tension, ν the liquid kinematic viscosity, a the acceleration due to external fields. In practical applications, involving the motion of small liquid droplets across a continuum gaseous phase, the Weber and Reynolds numbers can reach up to several thousands. It is therefore of interest to provide a semi-quantitative assessment of the capability of the present methods to reach up these parametric regimes. To this purpose, we remind the main limitations inherent to the LB models:

- $U_{lb}\lesssim0.1$ (finite-compressibility constraint);
- $\nu_{lb}\lesssim10^{-2}$ (dissipative stability constraint);
- $\nu_{pp}\sim1/6$ (stability constraint);
- $\sigma_{fe}\lesssim10^{-3}$ (surface tension stability constraint);
- $\sigma_{pp}\sim10^{-2}$ (EOS constraint).

The first constraint stems from the fact that LB is a weakly-compressible scheme, and if the local flow speed gets in the proximity of the sound speed c_s, the LB local equilibria may become negative, thereby ruining the stability of the scheme. The constraint on ν is related to the fact that if the viscosity becomes too low, typically 0.01 in lattice units with a grid of order $\mathcal{O}(100)$ lattice sites, local gradients of the flow field can develop, which may

undermine the very basis of the hydrodynamic limit, namely a weak departure from local equilibria (the above constraint is considerably relaxed by the so-called entropic version of LB methods [45, 46]). On the other hand, in the PP methods, the kinematic viscosity is numerically tightly close to $1/6$ (corresponding to $\tau = 1$), for reasons of numerical stability associated with higher order viscosity effects on the capillary force. The above constraints are well known from the single-phase LB literature [15].

The constraint on σ is inherent to the different formulations for non-ideal fluids. The EOS in the Shan-Chen approach fixes the surface tension magnitude to the density ratio, while in the $2-belt$ schematization, a certain degree of freedom in surface tension magnitude is allowed (see, for example, Table 1). Since in order to produce a phase transition, the non-ideal amplitude must exceed a given density threshold

$$|G| > G_{crit} = 4,$$

the resulting surface tension, proportional to G itself, cannot be made too small, typically not below 0.01. As to the FDFE method, a reciprocal constraint seems to apply.

Our direct numerical experience shows that it is very hard to bring the surface tension above $\sigma \sim 10^{-3}$ without experiencing numerical instabilities. This is certainly related to the specific structure of the finite-difference scheme, although we are not aware of any detailed analysis of this aspect. It is of interest to observe that this value is about ten times smaller than the typical surface tensions obtained with the (standard) Shan-Chen model [40]. Thus, starting from the above constraints, a reference resolution of 1000×1000 grid points, permits to explore approximately the following qualitative range of parameters:

$$Re_{pp} = \frac{U_{lb} D_{lb}}{\nu_{pp}} \lesssim 100, \qquad Re_{fe} = \frac{U_{lb} D_{lb}}{\nu_{fe}} \lesssim 1000, \tag{5.1a}$$

$$We_{pp} = \frac{\rho_{pp} U_{lb}^2 D_{lb}}{\sigma_{fe}} \lesssim 100, \qquad We_{fe} = \frac{\rho_{fe} U_{lb}^2 D_{lb}}{\sigma_{fe}} \lesssim 1000, \tag{5.1b}$$

$$Eo_{pp} = \frac{a_{lb} D_{lb}^2 \Delta\rho_{pp}}{\sigma_{pp}} \lesssim 10, \qquad Eo_{fe} = \frac{a_{lb} D_{lb}^2 \Delta\rho_{fe}}{\sigma_{fe}} \lesssim 100, \tag{5.1c}$$

$$Fr_{pp} = \frac{U_{lb}}{\sqrt{g_{lb}\ D_{lb}}} \lesssim 10, \qquad Fr_{fe} = \frac{U_{lb}}{\sqrt{g_{lb}\ D_{lb}}} \lesssim 10. \tag{5.1d}$$

If only qualitative, this set of values appears to be adequate for a broad range of multiphase applications.

6 Three-dimensional extensions

The extension of PP and FE methods to three dimensional flows does not pose any conceptual problem. However, the computational demand is obviously much higher, both

in terms of CPU-time and memory allocation. Ordinary three-dimensional LB simulations of non-ideal fluids run on grids of the order of $1-10$ millions grid points. Most advanced technological problems demand higher resolution, easily in the order of hundreds of millions lattice nodes on a uniform grid, which can only be accommodated through massively parallel implementations [48–52] and/or local grid-refinement [53, 54]. A few qualitative numbers help fixing ideas on the computational demand of three-dimensional LB applications. The performance of LB codes is often measured in so-called *MLUPS*, i.e., Millions of Lattice Updates per Second. Given that a plain LB solver involves of the order of 200 flops (floating point operations) to update a single lattice site, a performance of 10 MLUPS, i.e., 1 CPU second to update a 10-million grid, corresponds to roughly 2 Gflop/s, in standard units. With such a performance, a simulation covering, say 10^5 time-steps, would last roughly 1 CPU-day, which appears to be a reasonable figure for most practical purposes. For non-ideal LB schemes, the computational load is clearly higher, since additional operations are spent to compute the non-ideal interactions, whatever form they take in the actual implementation. In this respect, the FDFE appears to be substantially more demanding than PP and FE, not only because of additional operations, but mostly account on the substantial number of auxiliary variables that need to be stored to perform the computation. Leaving aside technical details, one can roughly estimate a factor 2-5 overhead in going from plain to non-ideal hydrodynamics. As a result, an application involving, say 100 million grid points, running at 10 MLUPS, would take weeks CPU-time to perform hundreds of thousands time-steps. These figures convey a precise feeling for the need of qualitatively new strategies, i.e., parallel computing and/or grid refinement, possibly a combination of the two. Clearly, this takes LB in a highly specialized and technical territory, for which the justly heralded LB "logo" of *simple models of complex fluids* goes definitely under question. This is no surprise, simply a standard "no free lunch" story.

As an example of an intensive 3D simulation using the LB-PP method, in Fig. 5 we report the liquid density capillary front propagating in a three-dimensional micro-channel. The main parameter are as follows: $G_0=-5$, $\rho_l=1.93$, $\rho_g=0.156$, $\sigma=0.06$ and $\nu=1/6$.

The simulation was performed on a grid of 7.5×10^6 lattice nodes, over 10^6 time-steps, covering a spatial domain of 70 microns in length and 11 microns in height and a time-span of about one millisecond. The overall simulation, which was run on a cluster of 8 Intel processors, takes about 5 CPU days elapsed time.

Another example of massively parallel application of the LB-PP method is presented in Fig. 6, where we show the density configuration corresponding to a liquid jet break-up at $We_l=38$. The main parameters are as follows: $G_0=-6$, $\rho_l=2.7$, $\rho_g=0.102$, $\sigma=0.16$. Note that, in order to obtain $We_l=38$, a very fine mesh must be used ($\Delta x=1\mu m$), which would require a grid of about 70×10^6 lattice nodes on a uniform mesh. In order to decrease this number of nodes, a mesh refinement technique is adopted; in particular the finer mesh ($\Delta x=1\mu m$) is used only in the region where the liquid jet develops. Using this approach, the number of nodal points reduces to about 20×10^6.

From Fig. 6, one can appreciate that the separated droplet is larger than the nozzle

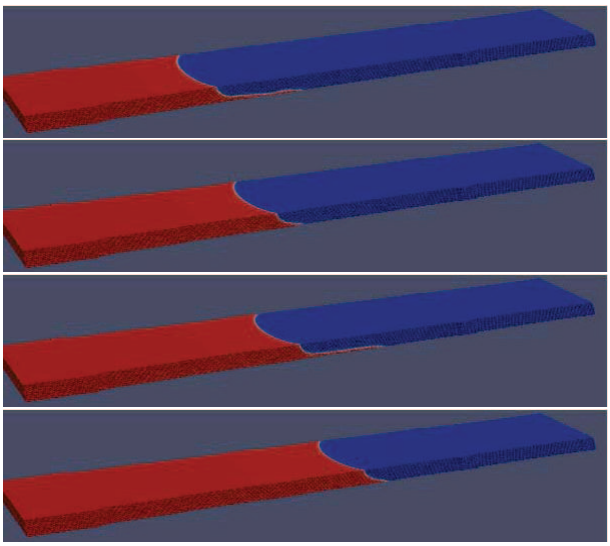

Figure 5: Penetration of the capillary front from left to right at four different instants in the filling process, $t=0.06$, 0.12, 0.15 and 0.27 milliseconds. Red and blue code for liquid and vapour phases, respectively.

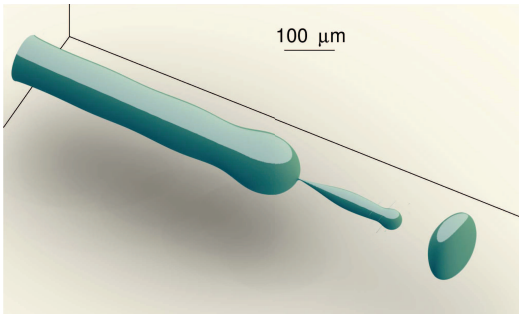

Figure 6: Liquid jet break-up at $We_l=38$.

radius, which is approximately equal to the jet radius. This is in line with experimental observations. Moreover a second, elongated droplet is also observed in between the jet and the disk-shaped droplet ahead. This intermediate droplet undergoes a rapid deformation towards a disk-spherical shape.

7 The front-tracking approach

As shown in the previous section, the *PP* and the *FDFE* approaches suffer of a number of limitations in simulating large-scale multiphase flows. As per the *FE* method, Eqs. (5.1a) and (5.1b) highlight tight limits in terms of Reynolds and Weber numbers which can be simulated free of numerical instabilities. As discussed earlier on in this paper, some of these limitations are inherent to the diffuse-interface nature of both methods.

One way of upscaling the physical size of the problem is to resort to front-tracking formulation, whereby the interface is treated as a zero-thickness, mathematical surface, across which the density field jumps from the light to the dense phase and viceversa. The FT model uses a simplified approach for the study of the interface between two immiscible fluids, based on the same philosophy of the VOF (Volume of Fluid) technique [55,56]. The main difference, which also represents the main advantage of the LBM front-tracking approach, is that the single-species transport equation, used in Navier-Stokes/VOF model to determine the relative volume fraction of the two phases, or phase fraction, in each computational cell, is not needed, since the free-surface tracking is automatically performed by advancing the fluid. Details are described in the following. In the LBM front-tracking model, a single set of LB equations is solved for the heavy fluid, from now on referred to as *liquid*, while the light fluid (i.e., *gas*) is neglected altogether in the simulation (infinite density ratio). This is consistent with the general spirit of the FT method, which does not aim at providing any description of the physics of the phase-transition between the two phases. The front is tracked through an additional variable, the liquid volume fraction, defined as follows:

$$\begin{cases} \varepsilon(x)=0, & \forall\, x\in G, \\ \varepsilon(x)=1, & \forall\, x\in L, \\ 0<\varepsilon(x)<1, & \forall\, x\in I. \end{cases}$$

In the above, G,L,I denotes the gas (i.e., empty cells), liquid and $interface$ cells, respectively. The domain is then composed of liquid, gas and interface cells. The latter contain both liquid and gas, and form a closed layer (buffer) between liquid and gas cells. This layer defines the free-surface to be tracked throughout the computational domain. Only a single layer of interface cells around the fluid cells is used. The computation splits into the following three steps [57,58]:

1. Interface motion;
2. Boundary conditions at the interface between gas and liquid;
3. Cell-type update.

7.1 Interface motion

The motion of the fluid interface is retrieved by means of the mass contained in the cell, i.e., by taking into account both the mass m and the fluid fraction ε of the cell, as follows:

$$m(\boldsymbol{x},t)=\varepsilon(\boldsymbol{x},t)\rho(\boldsymbol{x},t), \tag{7.1}$$

where the cell volume (area in two dimensions) is unity in LB units. The interface motion is computed from the mass flux between the cells: the evolution of mass is dictated by the

values of the populations streaming between two adjacent cells along all lattice directions connecting the two cells. For an interface cell located at $\boldsymbol{x}$ at time t, the mass change due to the streaming of the α-th population is given by:

$$\Delta m_\alpha(\boldsymbol{x},t) = C_\epsilon\left(f_\alpha^{pc}(\boldsymbol{x}+\boldsymbol{c}_\alpha\Delta t,t) - f_\beta^{pc}(\boldsymbol{x},t)\right), \tag{7.2}$$

where β is the mirror partner of α (i.e., $\boldsymbol{c}_\beta+\boldsymbol{c}_\alpha=0$) and C_ϵ is equal to 0, 1 or

$$\frac{\varepsilon(\boldsymbol{x}+\boldsymbol{c}_\alpha\Delta t,t)+\varepsilon(\boldsymbol{x},t)}{2},$$

depending on whether the cell centered at $\boldsymbol{x}+\boldsymbol{c}_\alpha\Delta_t$ is gas, liquid or interface cell. Superscript *pc* stands for post-collisional state.

From Eq. (7.2) we see that the amount of fluid leaving the cell is the same as the one entering the cell, for the sake of continuity. The time evolution of mass (and ϵ) reads as follows

$$m(\boldsymbol{x},t+\Delta t) = m(\boldsymbol{x},t) + \sum_\alpha \Delta m_\alpha(\boldsymbol{x},t). \tag{7.3}$$

If $\epsilon<0$ or $\epsilon>1$, the cell becomes a gas or a liquid cell, respectively. Note that direct changes from liquid to gas and viceversa are not permitted. Hence, liquid and gas cells are only allowed to transform into interface cells, whereas interface cells can transform into both gas and liquid cells. Finally, in the interfacial cells, mass and density are completely decoupled, so that the mass evolution does not affect the particle distribution functions.

7.2 Free-surface boundary conditions

Empty cells are never accessed during the computation. As a result, during the streaming process, only the particle distribution functions coming from liquid or interface cells can be computed, while those coming from the gas phase must be reconstructed from the boundary conditions at the liquid interface. At this stage, two major assumptions are made:

- The viscosity of the fluid is significantly lower than that of the gas phase;
- The gas pressure (i.e., atmospheric pressure) is constant.

The above corresponds to postulating that the interface moves the same way as the liquid does. At the boundary between the phases (i.e., interphase), the velocity of both is set to be the same and the force exerted by the gas is exactly in balanced with the one due to the liquid. The reconstruction procedure [57] provides the missing populations: for an interface cell at site $(\boldsymbol{x})$ with an empty cell at $(\boldsymbol{x}+\boldsymbol{c}_\alpha\Delta t)$, the post-streaming density function $\tilde{f}_\alpha$ is given by [59]

$$\tilde{f}_\alpha(\boldsymbol{x},t+\Delta t) = f_\alpha^{eq}(\rho_{gas},\boldsymbol{u}) + f_\beta^{eq}(\rho_{gas},\boldsymbol{u}) - f_\alpha(\boldsymbol{x},t), \tag{7.4}$$

where $\boldsymbol{u}$ is the fluid velocity at the interface cell. In Eq. (7.4), the effects of surface tension are neglected, but they may be included in the two equilibrium distribution functions [58, 59].

7.3 Cell-type updating

The collision step follows the same rules as in the *traditional* Lattice Boltzmann methods. Once the streaming and collision steps are completed, the cell type at the interface are checked for identity assignment: the conversion between gas and liquid is accomplished by accessing neighbouring cells and inspecting the following two conditions:

- The layer of the new interface must be closed again, to separate the two phases;
- Mass must be conserved during the conversion.

The density, calculated after the collision, is used to check whether the interface cell is to be filled or emptied during the time step:

$$m(\boldsymbol{x},t+\Delta t) > (1+k)\rho(\boldsymbol{x},t+\Delta t) \ \rightarrow \text{cell filled}, \tag{7.5a}$$

$$m(\boldsymbol{x},t+\Delta t) < (0-k)\rho(\boldsymbol{x},t+\Delta t) \ \rightarrow \text{cell emptied}, \tag{7.5b}$$

where k is an offset, usually $k=10^{-3}$.

In order to ensure mass conservation, the excess-mass is equally redistributed among the neighbouring cells. The neighborhood of all filled cells is then updated; the neighboring empty cells are turned into interface and initialized with the equilibrium distribution functions, computed with average density and velocity.

7.4 Front-tracking LB: simulations and results

To check the ability of the above algorithm to model extreme-wave conditions, a breaking dam problem was simulated and compared against experimental measurements from a wave tank. The test case is an experimental dam break over a triangular obstacle performed at the Université Catholique de Louvain (UCL) [60]. The experimental setup consists of a closed rectangular channel 5.6m long and 0.5m wide, with glassy walls. The upstream reservoir extends over 2.39m and is initially filled with 0.111m of water at rest. Downstream from the gate, a symmetrical bump 0.065 high with a bed slope of 0.014 is placed. The obstacle and the end walls define a second pool, which contains 0.025m of water (see Fig. 7). The gate separating the reservoir from the channel is pulled-up rapidly, causing the water block to disintegrate thereby generating a fast-running wave.

The gravity force effect has been incorporated into the LBM front-tracking simulation with a modified velocity into the local equilibrium [61].

The numerical contour plots, compared with pictures from the experimental results, show good agreement with the experimental behaviour, as shown in Figs. 8 and 9.

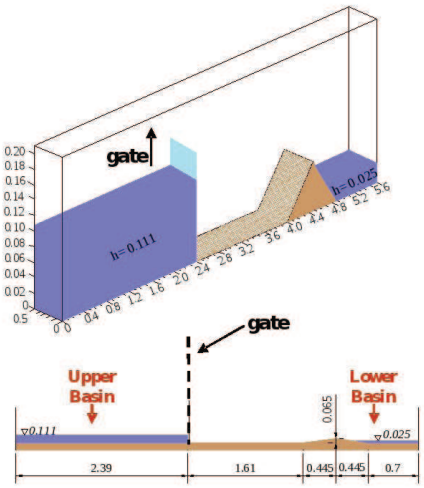

Figure 7: Experimental set-up and initial conditions for the dam break test case, all dimensions in meter.

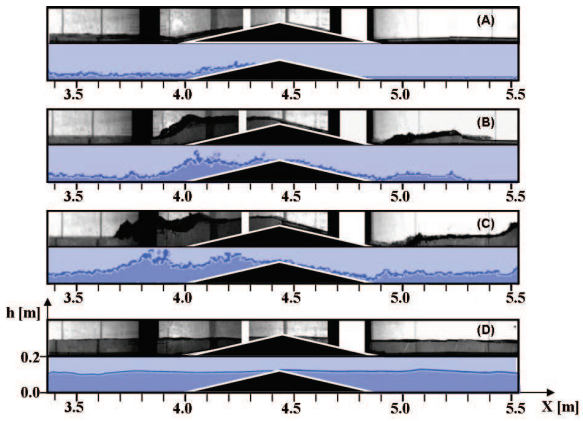

Figure 8: Real dam break profiles (picture) and simulation results (blue): (A): $t=1.8$s, (B): $t=3$s, (C): $t=3.7$s and (D): $t=8.4$s.

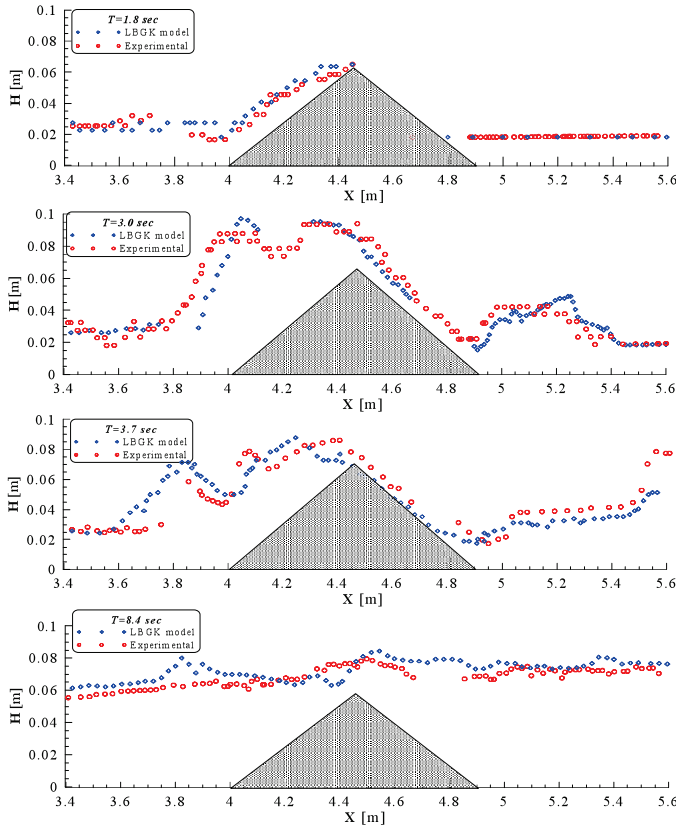

Figure 9: Comparison between computed and experimental results at several times after dam break: from top to bottom, $t=1$,8s; $t=3$s; $t=3.7$s; $t=8.4$s. Red dots: experimental data; blue diamonds: simulations.

8 Models range of application

It is of interest to compare the capabilities of the above three methods for the simulation of practical multiphase problems in different scientific/technological contexts. The *Front-Tracking* approach is best suited to the simulation of *macroscopic* phenomena, in which fluid *inertia* plays a dominant role. A typical field of application is *free-surface* phenomena, like tsunami's, flood waves or tidal waves, characterized by *Re* numbers well in excess of 10^4. Clearly, at such high-Reynolds numbers, the fluid solver must be supplemented with some form of turbulence modeling [62]. The *Pseudo-Potential* and the *FDFE* methods, on the other hand, are suited for phenomena from a *micro-* to a *meso-scale*, where the essential features of the physics of phase-transition are retained, although not down to the molecular scale (see cautionary remarks on the effects of finite-width interfaces). For sake of illustration, a free-jet simulation is described: Table 1 presents the main dimensionless parameters related to such case. The inlet velocity is set to 200m/s, that is 0.1 expressed in lattice units and the characteristic length is the nozzle diameter of 0.1mm, fixed to 200 lattice points for the different cases.

Table 1: Main parameters for a Diesel injection simulation; $u_{in}=0.1$ corresponding to $\sim$200m/s; densities and surface tension are expressed in lattice units.

	ρ_L	ρ_V	σ	Re_L	We_L	spurious currents
$PPSC$	2.5	0.083	0.1130	120	44.2	0.025
$PP2-belts$	2.5	0.083	$0.1009-0.1662$	120	$49.55-30.0$	$0.045-0.004$
$FDFE$	1	0.033	$1\,10^{-4}$	1200	$2\,10^4$	10^{-14}

The Re_L and We_L numbers in Table 1 can be increased only by decreasing the lattice spacing that is, increasing the number of nodes inside the domain, thus demanding higher computational efforts.

The boundary between the application fields of these two methods can be identified according to the magnitudes of the dimensionless numbers in Table 1. The FDFE approach allows to reach higher dimensionless numbers, due to its numerical stability in dealing with low viscosities ($\mathcal{O}(10^{-2})$ in lattice units) and *very* low surface tensions ($\mathcal{O}(10^{-4})$ in lattice units).

The Pseudo-Potential approach, on the other hand, has its viscosity numerically fixed tightly around ($\mathcal{O}(10^{-1})$ in lattice units) and surface tension ranging in an interval of $\mathcal{O}(10^{-2})/\mathcal{O}(10^{-1})$ lattice units. As a result, it appears more oriented towards micro-flow simulations, for which surface tension interactions play a dominant role.

As discussed earlier on in this paper, the main problem of the Pseudo-Potential methods is related to the presence of the spurious currents. However, these can be decreased in the $2-belt$ model by almost an order of magnitude [18]. As to the FDFE approach, the lack of suitable boundary conditions for solid-walls is setting a very stringent limitation to its applicability to many technological problems.

Table 2 proposes a possible (qualitative) way to distinguish the different fields of ap-

Table 2: Prospective application fields of the different LB multiphase methods as functions of the dimensionless numbers *Reynolds*, *Weber* and *Froude*, characterizing real-scale phenomena.

	$\frac{\rho_L}{\rho_V}$	Re_L	We_L	Fr	applications
$Front-Tracking$	$-$	$>10^4$	$>10^6$	$<10^1$	large-scale hydraulics high-speed sprays
$FDFE$	10^3	$<10^4$	$>10^3$	$>10^2$	free jets cavitation
$PP2-belts$	10^2	$<10^3$	$<10^3$	$>10^0$	wall impingement low-speed jets
$PPSC$	10^1	$<10^2$	$<10^2$	$>10^0$	micro-flows ferrofluids capillarity effects

plication of the different methods, as referred to the order of magnitude of the main dimensionless parameters characterizing the *real* phenomena (that is, referring to physical units instead of lattice ones). It is worth noting that a *We* range has been indicated also for the front tracking approach, mainly suitable for large scale hydraulics, characterized by high *Re* and low *Fr*, not reachable by the SC and free-energy models. In fact, in the application shown in the front-tracking section, the surface tension is neglected altogether. However, the front-tracking method may be also applied to those flow problems, such as free-jet or droplet flows, in which surface tension plays a significant role at the interface. To this end, the Young-Laplace equation (i.e., surface tension, local interface curvature and liquid- and gas-side pressure effects) must be included as an external force term in Eq. (7.4), as reported in [58].

9 Conclusions

Summarizing, we have discussed three major variants of the lattice Boltzmann method for non-ideal fluids, i.e., the pseudo-potential, free-energy and front-tracking approaches. Each of them comes with specific merits and drawbacks, which means that a clearcut separation between the respective domains of applicability can only be drawn on qualitative grounds. Nevertheless, we hope and believe that the qualitative criteria presented in this paper, and the accompanying numerical evidence, may provide a useful guideline for prospective users of the Lattice Boltzmann method in the field of multiphase flow simulations. This paper makes no claim of generality beyond those suggested by the direct, hence limited, experience of the present authors.

References

[1] A. Prosperetti and G. Tryggvason, Computational Methods for Multiphase Flow, Cambridge University Press, 2005.
[2] D. Grunau, S. Chen and K. Eggert, A lattice Boltzmann model for multiphase fluid flows, Phys. Fluids. A., 5 (1993), 2557–2562.
[3] J. Eggers, Nonlinear dynamics and breakup of free-surface flows, Rev. Mod. Phys., 69 (1997), 865–927.

[4] A. K. Gunstensen, D. H. Rothman, S. Zaleski and G. Zanetti, Lattice Boltzmann model of immiscible fluids, Phys. Rev. A., 43 (1991), 4320–4327.
[5] A. K. Gunstensen and D. H. Rothman, Microscopic modeling of immiscible fluids in three dimensions by a lattice Boltzmann method, EPL., 18 (1992), 157–161.
[6] D. H. Rothman and J. M. Keller, Immiscible cellular-automaton fluids, J. Stat. Phys., 52 (1988), 1119–1127.
[7] S. Succi, O. Filippova, G. Smith and E. Kaxiras, Applying the Lattice Boltzmann equation to multiscale fluid problems, Computing in Science and Engineering, 3 (2001), 26-37.
[8] D. D'Humieres, Y. H. Qian and P. Lallemand, Lattice BGK Models for Navier-Stokes equation, EPL., 17(6) (1992), 479–484.
[9] S. Succi, The Lattice Boltzmann Equation: for Fluid Dynamics and Beyond, Series Numerical Mathematics and Scientific Computation, Oxford University Press, 2001.
[10] Shan. X. and Chen. H, Lattice Boltzmann model for simulating flows with multiple phases and components, Phys. Rev. E., 47 (1993), 1815–1820.
[11] Shan. X. and Chen. H, Simulation of nonideal gases and liquid-gas phase transitions by the lattice Boltzmann equation, Phys. Rev. E., 49 (1994), 2941–2948.
[12] F. Diotallevi, L. Biferale, S. Chibbaro and S. Succi, Lattice Boltzmann simulation of capillary filling: finite vapour density effects, Euro. Phys. J. Spec. Top., 171 (2009), 237–243.
[13] C. Biscarini, S. Di Francesco and P. Menciola, CFD modelling approach for dam break flow studies, Hydrol. Earth. Syst. Sci. Discuss., 6 (2009), 6759–6793. Lattice Boltzmann Modeling: An Introduction for Scientists and Engineers, Springer Verlag, New-York, 2006.
[14] C. Biscarini, S. Di Francesco, M. Mencattini and L. Pizzuto, Free surface lattice Boltzmann method for hydraulic problems, Acta of the First International Conference on Computational Methods for Thermal Problems, 129–132, ThermaComp2009, Naples, Italy.
[15] G. Falcucci, G. Bella, G. Chiatti, S. Chibbaro, M. Sbragaglia and S. Succi, Lattice Bolzmann models with mid-range interactions, Commun. Comput. Phys., 2(6) (2007), 1071–1084.
[16] M. Sbragaglia, R. Benzi, L. Biferale, S. Succi, K. Sugiyama and F. Toschi, Generalized lattice Boltzmann method with multirange pseudopotential, Phys. Rev. E., 75 (2007), 026702.
[17] G. Falcucci, G. Chiatti, S. Succi, A. Kuzmin and A. M. Mohamad, Rupture of a ferrofluid droplet in external magnetic fields using a single-component lattice Boltzmann model for nonideal fluids, Phys. Rev. E., 79 (2009), 056706.
[18] G. Falcucci, S. Succi and S. Ubertini, Lattice Boltzmann simulations of phase-separating flows at large density ratioes: the case of doubly-attractive pseudo-potentials, submitted.
[19] C. Clanet, C. Bguin, D. Richard and D. Qur, Maximal deformation of an impacting drop, J. Fluid. Mech., 517 (2004), 199–208.
[20] S. Chibbaro, G. Falcucci, G. Chiatti, H. Chen, X. Shan and S. Succi, Lattice Boltzmann models for non-ideal fluids with arrested phase-separation, Phys. Rev. E., 77 (2008), 036705.
[21] G. Falcucci, S. Chibbaro, S. Succi, X. Shan and H. Chen, Lattice Boltzmann spray-like fluids, EPL., 82 (2008), 24005.
[22] L. S. Luo and S. S. Girimaji, Theory of the lattice Boltzmann method: two-fluid model for binary mixtures, Phys. Rev. E., 67 (2003), 036302.
[23] M. R. Swift, E. Orlandini, W. R. Osborn and J. M. Yeomans, Lattice Boltzmann simulations of liquid-gas and binary fluid systems, Phys. Rev. E., 54 (1996), 5041–5052.
[24] D. Jacqmin, Calculation of two-phase Navier-Stokes flows using phase-field modeling, J. Comput. Phys., 155 (1999), 96–127.
[25] M. Sbragaglia, H. Chen. X. Shan and S. Succi, Continuum free-energy formulation for a class of lattice Boltzmann multiphase models, EPL., 86(2) (2009), 24005.

[26] E. Orlandini, M. R. Swift and J. M. Yeomans, A lattice Boltzmann model of binary-fluid mixtures, EPL., 32 (1995), 463.
[27] M. R. Swift, W. R. Osborn and J. M. Yeomans, Lattice Boltzmann simulation of nonideal fluids, Phys. Rev. Lett., 75 (1995), 830–833.
[28] G. Gonnella, E. Orlandini and J. M. Yeomans, Lattice Boltzmann simulations of lamellar and droplet phases, Phys. Rev. E., 58 (1998), 480–485.
[29] A. Lamura, G. Gonnella and J. M. Yeomans, A lattice Boltzmann model of ternary fluid mixtures, EPL., 45 (1999), 314.
[30] A. Xu, G. Gonnella and A. Lamura, Phase separation of incompressible binary fluids with lattice Boltzmann methods, Phys. A. Stat. Mech. App., 331(1-2) (2004), 10–22.
[31] V. Sofonea, A. Lamura, G. Gonnella and A. Cristea, Finite-difference lattice Boltzmann models with flux limiters for liquid-vapor systems, Phys. Rev. E., 70 (2004), 046702.
[32] A. J. Wagner and C. M. Pooley, Interface width and bulk stability: requirements for the simulation of deeply quenched liquid-gas systems, Phys. Rev. E., 76 (2007), 045702(R).
[33] Z. Guo, C. Zheng and B. Shi, Discrete lattice effects of the forcing term in the lattice Boltzmann method, Phys. Rev. E., 65 (2004), 046308.
[34] J. Becker, M. Junk, D. Kehrwald, G. Thömmes and Z. Yang, A combined lattice BGK/level set method for immiscible two-phase flows, Comput. Math. Appl., 58 (2009), 950–964.
[35] A. L. Kupershtokh, D. A. Medvedev and D. I. Karpov, On equations of state in a lattice Boltzmann method, Comput. Math. Appl., 58 (2009), 965–974.
[36] T. Lee and C.-L. Lin, A stable discretization of the lattice Boltzmann equation for simulation of incompressible two-phase flows at high density ratio, J. Comput. Phys., 206 (2005), 16–47.
[37] T. Lee and P. F. Fischer, Eliminating parasitic currents in the lattice Boltzmann equation method for nonideal gasses, Phys. Rev. E., 74 (2006), 046709.
[38] T. Lee, Effects of incompressibility on the elimination of parasitic currents in the lattice Boltzmann equation method for binary fluids, Comput. Math. Appl., 58(5) (2009), 987–994.
[39] T. Lee and L. Liu, Wall boundary condition in the lattice Boltzmann equation method for nonideal gasses, Phys. Rev. E., 78 (2008), 017702.
[40] D. Chiappini, G. Bella, S. Succi, F. Toschi and S. Ubertini, Improved lattice Boltzmann without parasitic currents for Rayleigh-Taylor instability, Commun. Comput. Phys., 7 (2010), 423–444.
[41] D. Chiappini, G. Bella, S. Succi, F. Toschi and S. Ubertini, Application of finite difference lattice Boltzmann method to break-up and coalescence in multiphase flows, Int. J. Mod. Phys. C., 20-11 (2009), 1803.
[42] X. He, S. Chen and R. Zhang, A lattice Boltzmann scheme for incompressible multiphase flow and its application in simulation of Rayleigh-Taylor instability, J. Comput. Phys., 152 (1999), 642–663.
[43] R. R. Nourgaliev, T. N. Dinh and T. G. Theofanous, A pseudocompressibility method for the numerical simulation of incompressible multifluid flows, Int. J. Multiphase. Flows., 30 (2004), 901–937.
[44] W. H. Cabot and A. W. Cook, Reynolds number effects on Rayleigh-Taylor instability with possible implications for type-Ia supernovae, Nat. Phys., 2 (2006), 562–568.
[45] I. V. Karlin, A. Ferrante and H. C. Ottinger, Perfect entropy functions of the lattice Boltzmann method, EPL., 47 (1999), 182–188.
[46] B. M. Boghosian, P. J. Love, P. V. Coveney et al., Galilean-invariant lattice-Boltzmann models with H theorem, Phys. Rev. E., 68 (2003), 025103R.
[47] Z. Huang, A. De Luca, T. J. Atherton, M. Bird and C. Rosenblatt, Rayleigh-Taylor instability

experiments with precise and arbitrary control of the initial interface shape, Phys. Rev. Lett., 99 (2007), 204502.
[48] G. Amati, S. Succi and R. Piva, Massively parallel lattice-Boltzmann simulation of turbulent channel flow, Int. J. Mod. Phys. C., 8 (1997), 869–877.
[49] D. Kandhai, A. Koponen, A. G. Hoekstra et al., Lattice-Boltzmann hydrodynamics on parallel systems, Comput. Phys. Commun., 111 (1998), 14–26.
[50] J. C. Desplat, I. Pagonabarraga and P. Bladon, LUDWIG: A parallel Lattice-Boltzmann code for complex fluids, Comput. Phys. Commun., 134 (2001), 273–290.
[51] M. D. Mazzeo and P. V. Coveney, HemeLB: A high performance parallel lattice-Boltzmann code for large scale fluid flow in complex geometries, Comput. Phys. Commun., 178 (2008), 894–914.
[52] M. Bernaschi, S. Melchionna, S. Succi et al., MUPHY: A parallel multi physics/scale code for high performance bio-fluidic simulations, Comput. Phys. Commun., 180 (2009), 1495–1502.
[53] A. Dupuis and B. Chopard, Theory and applications of an alternative lattice Boltzmann grid refinement algorithm, Phys. Rev. E., 67 (2003), 066707.
[54] B. Crouse, E. Rank, M. Krafczyk et al., A LB-based approach for adaptive flow simulations, Int. J. Mod. Phys. B., 17(1-2) (2003), 109–112.
[55] C. W. Hirt and B. D. Nichols, Volume of fluid method for dynamics of free boundaries, J. Comput. Phys., 30 (1981), 201–221.
[56] R. Scardovelli and S. Zaleski, Direct numerical simulation of free-surface and interfacial flow, Annu. Rev. Fluid. Mech., 31 (1999), 567–603.
[57] C. Körner, M. Thies, T. Hofmann, N. Thürey and U. Rüde, Lattice Boltzmann model for free surface flow for modeling foaming, J. Stat. Phys., 121(1/2) (2005), 179–196.
[58] N. Thürey, U. Rüde and C. Körner, Interactive free surface fluids with the lattice Botlzmann method, Technical Report 05-4, Lehrstuhl fur Informatik 10 (Systemsimulation), University of Erlangen-Nueremberg.
[59] N. Thürey and U. Rüde, Stable free surface flows with the lattice Boltzmann method on adaptively coarsened grids, Comput. Vis. Sci., 12 (2009), 247–263.
[60] Soarez Frazao, Dam-Break Induced Flows in Complex Topographies, Theoretical, Numerical and Experimental Approaches, PhD Thesis, Louvain-la-Neuve: Université Catholique de Louvain, Civil Engineering Department, Hydraulics Division, 2002.
[61] J. M. Buick and C. A. Greated, Gravity in a lattice Boltzmann model, Phys. Rev. E., 61 (2000), 5307.
[62] H. Chen, S. Kandasamy, S. Orszag, R. Shock, S. Succi and V. Yakhot, Extended Boltzmann kinetic equation for turbulent flows, Science., 301 (2003), 633–636.